

Mapping reionization bubbles in the JWST era II: inferring the position and characteristic size of individual bubbles

Ivan Nikolić¹, Andrei Mesinger¹, Charlotte A. Mason^{2,3}, Ting-Yi Lu^{2,3}, Mengtao Tang⁵, David Prelogović^{1,4}, Samuel Gagnon-Hartman¹, and Daniel P. Stark⁵

¹ Scuola Normale Superiore, Piazza dei Cavalieri 7, 56125 Pisa, PI, Italy

² Cosmic Dawn Center (DAWN)

³ Niels Bohr Institute, University of Copenhagen, Jagtvej 128, 2200 Copenhagen N, Denmark

⁴ Scuola Internazionale Superiore di Studi Avanzati (SISSA), Via Bonomea 265, 34136 Trieste, Italy

⁵ Steward Observatory, University of Arizona, 933 N Cherry Ave, Tucson, AZ 85721, USA

Received; accepted

ABSTRACT

The James Webb Space Telescope (*JWST*) is discovering an increasing number of galaxies well into the early stages of the Epoch of Reionization (EoR). Many of these galaxies are clustered with strong Lyman alpha ($\text{Ly}\alpha$) emission, motivating the presence of surrounding cosmic HII regions that would facilitate $\text{Ly}\alpha$ transmission through the intergalactic medium (IGM). Detecting these HII "bubbles" would allow us to connect their growth to the properties of the galaxies inside them. Here we develop a new forward-modeling framework to estimate the local HII region size and location from $\text{Ly}\alpha$ spectra of galaxy groups in the early stages of the EoR. Our model takes advantage of the complementary information provided by neighboring sightlines through the IGM. Our forward models sample the main sources of uncertainty, including: (i) the global neutral fraction; (ii) EoR morphology; (iii) emergent $\text{Ly}\alpha$ emission; and (iv) NIRSpec instrument noise. Depending on the availability of complementary nebular lines, $\sim 0.006 - 0.01$ galaxies per cMpc^3 , are required to be $\geq 95\%$ confident that the HII bubble location and size recovered by our method is accurate to within ~ 1 comoving Mpc. This corresponds roughly to tens of galaxies at $z \sim 7-8$ in $\sim 2 \times 2$ tiled pointing with *JWST* NIRSpec. Such a sample is achievable with a targeted survey with completeness down to $M_{\text{UV}}^{\text{min}} \lesssim -19 - -17$, depending on the over-density of the field. We test our method on 3D EoR simulations as well as misspecified equivalent width distributions, in both cases accurately recovering the HII region surrounding targeted galaxy groups.

Key words. Galaxies: high-redshift – intergalactic medium – Cosmology: dark ages, reionization, first stars

1. Introduction

The Epoch of Reionization (EoR) marks an important milestone in the Universe's evolution. UV radiation from the first, clustered galaxies reionized their surrounding intergalactic medium (IGM). These HII "bubbles" expanded, percolated, and eventually permeated all of space, completing the final phase change of our Universe. The timing and morphology of the EoR tell us which galaxies were responsible as well the role of IGM clumps that regulated the end stages (e.g., McQuinn et al. 2007; Sobacchi & Mesinger 2014).

Lyman α emission from galaxies is an especially useful tool for studying the early stages of the EoR, when HII regions are relatively small such that the neutral IGM leaves a strong imprint via damping wing absorption (e.g., see review in Dijkstra 2014). A common approach is to estimate the mean neutral fraction of the IGM using a statistically large sample of galaxies (e.g., Mesinger & Furlanetto 2008b; Stark et al. 2010; Mesinger et al. 2015; Mason et al. 2018; Jung et al. 2020; Bolan et al. 2022; Jones et al. 2024; Nakane et al. 2024). However, galaxies reside in biased regions of the IGM, and connecting the corresponding damping wing signature to the mean neutral fraction is very model dependent (e.g., Mesinger & Furlanetto 2008a; Lu et al. 2024a). In contrast, unbiased probes such as the Lyman alpha forest are sourced from representatively-large volumes of the IGM, and can already tightly constrain the mean neutral frac-

tion during the latter half of the EoR (Qin et al. 2021; Bosman et al. 2022; Qin et al. 2024).

In addition to estimating the *global* neutral fraction from the IGM $\text{Ly}\alpha$ damping wings, one could instead infer the presence (or lack thereof) of an *individual* HII region surrounding an observed group of galaxies (Tilvi et al. 2020; Endsley & Stark 2022; Jung et al. 2022; Hayes & Scarlata 2023). This could potentially allow us to connect the growth of the local HII region to the properties of the galaxies inside it. Having several such estimates of HII bubble sizes will allow us to understand which kind of galaxies drove reionization (e.g., faint/bright; McQuinn et al. 2007; Mesinger et al. 2016), well before the advent of tomographic 21cm maps with the Square Kilometer Array (SKA). Fortunately, the James Webb Space Telescope (*JWST*) is providing spectra from an ever-increasing number of galaxy groups at high redshifts which can be used for this purpose (e.g., Saxena et al. 2023; Witstok et al. 2024a; Tang et al. 2023, 2024b; Chen et al. 2024; Umeda et al. 2024; Napolitano et al. 2024).

However, the interpretation of these observations has so far been fairly approximate. The presence of an IGM damping wing in each galaxy is estimated *independently of its neighbors*. This wastes invaluable information, as neighboring galaxies provide complimentary sightlines into the local EoR morphology. The result is that the studies focusing on individual galaxies generally only predict lower limits for the radii of local HII regions. Furthermore, studies tend to ignore one or more important sources

of stochasticity in the EoR morphology, intrinsic galaxy emission and/or telescope noise.

In this work we develop a new framework to *infer the local HII region size and location* from Ly α observations of a galaxy group. Our formalism accounts for the *relative position* of each galaxy with respect to the host and nearby HII bubbles by creating self-consistent forward models of JWST/NIRSpec spectra for each galaxy. We account for the relevant sources of uncertainty/stochasticity, including: (i) the IGM mean neutral fraction, \bar{x}_{HI} ; (ii) the EoR morphology, given \bar{x}_{HI} ; (iii) the emergent Ly α emission, given the observed UV magnitudes; and (iv) NIRSpec instrument noise. Unlike many previous studies, we do not make any assumptions about the unknown relative contribution of observed versus unobserved galaxies to the growth of the local HII region. We quantify how many galaxies are required to robustly detect individual ionized regions with a $\lesssim 10\%$ accuracy in their inferred location and characteristic size, during the early stages of EoR. This work is a companion to [Lu et al. \(2024b\)](#), in which we presented a complementary formalism to detect edges of ionized regions, using empirically-calibrated relations.

This paper is structured as follows. In Section 2 we present our forward modeling pipeline for Ly α galaxy spectra during the EoR. We introduce our procedure to infer the size and location of the surrounding HII region in Section 3. We apply our framework to mock data and show our main results in Section 4. We build further confidence by performing out-of-distribution tests in Section 5. In Section 6 we quantify observational requirements for detecting individual HII regions and we conclude in Section 7. All quantities are presented in comoving units unless stated otherwise. We assume a standard Λ CDM cosmology ($\Omega_{\text{m}}, \Omega_{\text{b}}, \Omega_{\Lambda}, h, \sigma_8, n_s = 0.310, 0.049, 0.689, 0.677, 0.81, 0.963$), with parameters consistent with the latest estimates from [Planck Collaboration et al. \(2020\)](#). All quantities are quoted in comoving units and evaluated in the rest-frame, unless stated otherwise.

2. Observing Lyman alpha spectra from galaxies during the EoR

Our fiducial set-up is shown in Fig. 1. An HII region in an observed galaxy field is characterized as a sphere, with a center location (O_{b}) and characteristic radius (R_{b}). This is the "local" or "target" HII region whose properties we aim to infer. Nearby ionized regions are also shown in blue in the diagram. Observed galaxies can be located both inside and outside HII regions; here we denote three such galaxies with 'A', 'B', 'C', highlighting their sightlines towards the observer with red arrows.

Specifically, we wish to determine the conditional probability of the HII bubble center, O_{b} , and radius, R_{b} , given observed Ly α spectra of N_{gal} galaxies in a field with a central redshift z ,

$$\mathcal{P}(O_{\text{b}}, R_{\text{b}} | \mathbf{x}^i, f_{\alpha}^i(\lambda), M_{\text{UV}}^i, z), \quad i \in [1, N_{\text{gal}}] \quad (1)$$

Here \mathbf{x}^i , M_{UV}^i , and $f_{\alpha}^i(\lambda)$ are vectors of the galaxies' Cartesian coordinates, UV magnitudes, and observed Ly α spectra. For each galaxy, the observed spectrum in the rest-frame can be written as:

$$f_{\alpha}(\lambda) = L_{\alpha} J(\lambda) e^{-\tau_{\text{EoR}}(\lambda)} + \mathcal{N}(\lambda) \quad (2)$$

where L_{α} is the emergent¹ Lyman-alpha luminosity of a galaxy, $J(\lambda)$ is the normalized, emergent Lyman- α profile,

¹ Throughout we use the term "emergent" to refer to values escaping from the galaxy into the IGM. Therefore the emergent amplitude, L_{α} , and profile, $J(\lambda)$, are determined by Lyman alpha radiative transfer

$\exp[-\tau_{\text{EoR}}(\lambda)]$ accounts for IGM attenuation, and $\mathcal{N}(\lambda)$ is the spectrograph noise.

In the schematic shown in Fig. 1, galaxy 'A' is outside of an ionized bubble, and its Lyman α flux will therefore be strongly attenuated by the neutral IGM (i.e. having a large $\tau_{\text{EoR}}(\lambda)$). We should only detect Lyman alpha flux from galaxy 'A' if it has a high emergent luminosity, L_{α} , and its Ly α profile, $J(\lambda)$, is strongly redshifted from the systemic z (e.g., [Dijkstra 2014](#)). Galaxy 'B' is close to the center of the local HII bubble, and will have (*on average*; c.f. right panel of Fig. 5), the lowest Ly α damping wing attenuation from the patchy EoR. However, the observed flux depends on all of the terms in eq. (2), each of which can have sizable stochasticity. Below we detail how each of these terms.

2.1. emergent Lyman-alpha profile

We start with the Lyman-alpha profile emerging into the IGM, $J(\lambda)$, normalized to integrate to unity. In order to escape the ISM of the galaxy, Lyman- α photons must diffuse spectrally which leads to a double-peaked Lyman-alpha shape ([Neufeld 1990](#); [Hu et al. 2023](#); [Hutter et al. 2023](#); [Almada Monter & Gronke 2024](#)). Due to the resonant nature of the line, the blue peak generally gets absorbed even by the ionized IGM at $z \gtrsim 5$ (though see [Meyer et al. 2021](#) for some putative, rare counter examples). Following [Mason et al. \(2018\)](#), we model the remaining red peak as a Gaussian:

$$J(\lambda) = \frac{2}{v_{\alpha}} \sqrt{\frac{\ln 2}{\pi}} \exp\left(-\frac{(\Delta v - v_{\alpha})^2}{v_{\alpha}^2 / (2 \ln 2)}\right), \quad (3)$$

where v_{α} represents the velocity offset from systemic of the center of the line, and $\Delta v = ((\lambda - \lambda_{\alpha})c/\lambda_{\alpha})$ is the velocity difference from the resonant wavelength of the line, $\lambda_{\alpha} = 1215.16\text{\AA}$. As in [Mason et al. \(2018\)](#), for simplicity we assume that the FWHM of the line is equal to the velocity of the offset (e.g., [Verhamme et al. 2018](#)). Although these profiles are motivated by lower redshift observations (e.g. [Yamada et al. 2012](#); [Orlitoová et al. 2018](#); [Hu et al. 2023](#)), we note that our framework can easily accommodate any distribution for $J(\lambda)$, once we have better models for the emergent spectra. We also assume that all Lyman-alpha photons with a velocity offset below the circular velocity, v_{circ} , of the host halo are absorbed by the CGM ([Dijkstra et al. 2011](#); [Laursen et al. 2011](#)). In Fig. 2 we show an example of the emergent profile in blue, for a galaxy with UV magnitude $M_{\text{UV}} = -20.0$ and velocity offset $v_{\alpha} = 270\text{km/s}$, with a $v_{\text{circ}} = 160\text{km/s}$.

The PDF of the emergent velocity offset is well described by a log-normal distribution ([Steidel et al. 2014](#); [De Barros et al. 2017](#); [Stark et al. 2017](#); [Mason et al. 2018](#)):

$$\mathcal{P}(v_{\alpha} | M_{\text{UV}}) = \frac{1}{\sqrt{2\pi} \ln 10 v_{\alpha} \sigma_v} \exp\left(-\frac{(\log_{10} v_{\alpha} - \bar{v}_{\alpha}(M_{\text{UV}}))^2}{2\sigma_v^2}\right) \quad (4)$$

where the mean velocity offset is correlated with the UV magnitude ([Stark et al. 2017](#), though see [Bolan et al. \(2024\)](#)):

$$\log_{10} \bar{v}_{\alpha}(M_{\text{UV}}, z) = 0.32\gamma(M_{\text{UV}} + 20.0 + 0.26z) + 2.34 \quad (5)$$

through the interstellar medium (ISM) and the circumgalactic medium (CGM; e.g. [Neufeld 1990](#); [Laursen et al. 2011](#)). We do not model the details of this radiative transfer in this work, but instead rely on empirical relations based on post-EoR observations to determine the conditional distributions of L_{α} and $J(\lambda)$.

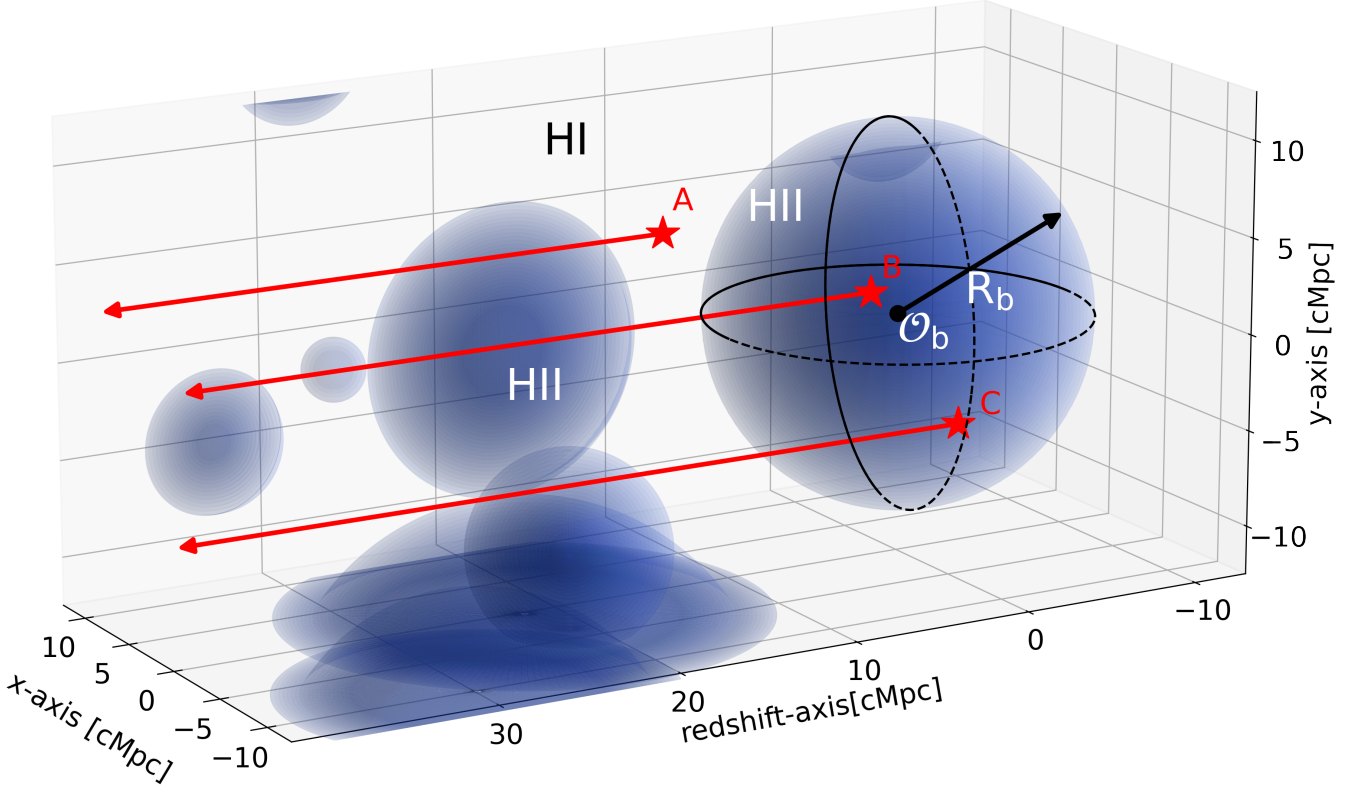


Fig. 1. Schematic of our framework. Cosmic HII regions are shown in blue, embedded in an otherwise neutral IGM. We observe Lyman alpha spectra from a group of galaxies (here three example galaxies are denoted with 'A', 'B', and 'C'), and we wish to infer the central HII bubble (characterized by a sphere with radius ' R_b ' and center ' O_b '). Our framework combines the complimentary information provided by neighboring sight-lines towards the galaxies (red arrows), accounting for the main sources of stochasticity.

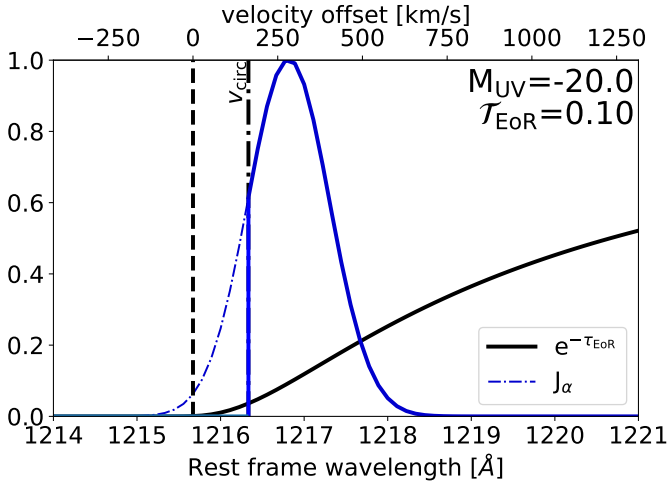


Fig. 2. An example of an emergent Lyman alpha line and IGM opacity as a function of wavelength. The blue solid line represents the normalized Lyman- α emergent profile, while the blue dot-dashed line demarcates the flux absorbed by the CGM, blueward of the circular velocity of the galaxy. The solid black line illustrates an IGM damping wing attenuation profile, taken from a random sightline at $\bar{x}_{\text{HI}} = 0.65$ and $R_b = 10\text{cMpc}$ (see text for details). The Lyman alpha transmission integrated over all wavelengths for this example would be $\mathcal{T}_{\text{EoR}} \equiv \int d\lambda J(\lambda) e^{-\tau_{\text{EoR}}(\lambda)} = 0.10$.

and $\sigma_v = 0.24$, $\gamma = -0.3$ for $M_{\text{UV}} \geq -20.0 - 0.26z$, and $\gamma = -0.7$ otherwise. We show this distribution in the upper panel of Fig. 3.

Although there is some indication of a mild redshift evolution in this distribution (e.g., Tang et al. 2024b; Witstok et al. 2024b), we show in Section 5 that our results are insensitive to such changes.

2.2. Emergent Lyman-alpha luminosity

The absolute normalization of the profile discussed above (i.e., the emergent Lyman alpha luminosity L_α) is generally defined via the so-called rest-frame equivalent width (e.g., Dijkstra & Wyithe 2012):

$$W = \frac{L_\alpha}{L_{1500,\nu}} \frac{\lambda_\alpha}{\nu_\lambda} \left(\frac{\lambda_{\text{UV}}}{\lambda_\alpha} \right)^{\beta+2} \quad (6)$$

where $L_{1500,\nu} [\text{erg/s/Hz}]$ is the specific UV luminosity evaluated at 1500\AA obtained from the continuum flux $f_{1500,\nu}$: $L_{1500,\nu} = 4\pi d_L^2 f_{1500,\nu}$ where $f_{1500,\nu}$ is given in units of $[\text{erg/s/cm}^2/\text{Hz}]$, where d_L is the luminosity distance to the source, $\nu_\lambda = 2.47 \times 10^{15} \text{Hz}$, $\lambda_\alpha = 1215.67\text{\AA}$, $\lambda_{\text{UV}} = 1500\text{\AA}$ is the rest-frame wavelength at which the UV magnitude is measured and β is the UV slope (which we assume to be $\beta = -2.0$ for simplicity).

For galaxies at $z < 6$, where we expect τ_{EoR} to be negligible, Mason et al. (2018) found the following fit based on data from De Barros et al. (2017):

$$p_6(W|M_{\text{UV}}) = \frac{A(M_{\text{UV}})}{W_c(M_{\text{UV}})} e^{-\frac{W}{w_c(M_{\text{UV}})}} H(W) + [1 - A(M_{\text{UV}})] \delta(W), \quad (7)$$

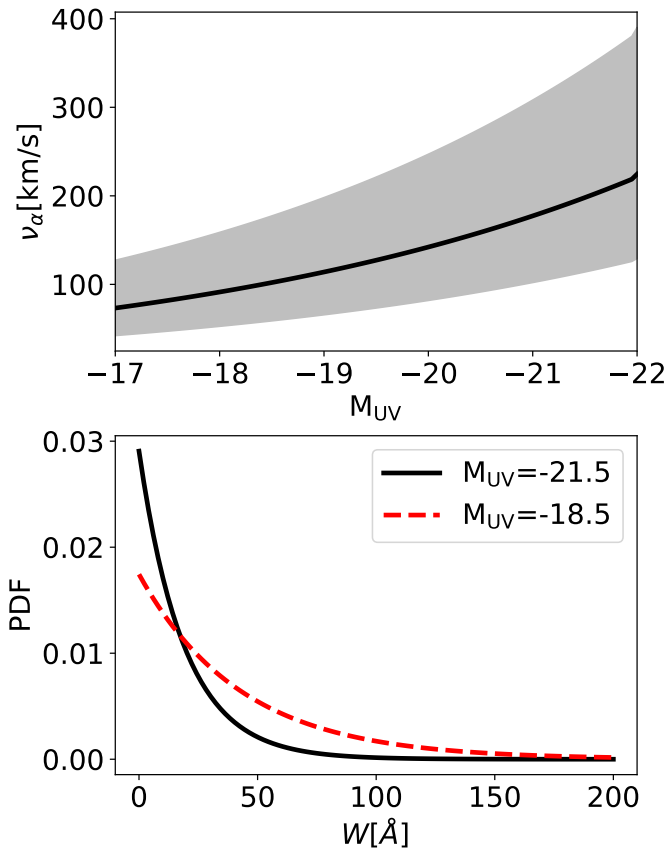


Fig. 3. *Upper panel:* Mean (black line) and 1-sigma (shaded region) of the velocity offset distribution as a function of UV magnitude (Eq. 4). *Lower panel:* PDF of the Lyman-alpha rest-frame equivalent widths. The black and red dashed curves represent the distribution of equivalent widths (W) for Lyman- α emitters (Eq. 7). The non-emitters have equivalent widths described by a delta-function at $W = 0\text{\AA}$ (not shown) normalized such that the integral of the PDF is 1. The distribution is shown for $M_{UV} = -18.5$ and -21.5 .

where $A(M_{UV})$ is the fraction of intrinsic emitters for a given M_{UV} and $W_c(M_{UV})$ is the characteristic scale of the distribution, which is anti-correlated with M_{UV} . $H(W)$ is the Heaviside step function and $\delta(W)$ is a Dirac delta function. We use the following fit, as in Mason et al. (2018): $A = 0.65 + 0.1 \tanh[3(M_{UV} + 20.75)]$ and $W_c = 31 + 12 \tanh[4(M_{UV} + 20.25)]\text{\AA}$. The distribution of emergent equivalent widths is shown in the lower panel of Figure 3 for two UV magnitudes. We note that our framework can easily accommodate different EW distributions (e.g., Treu et al. 2012; Lu et al. 2024b; Tang et al. 2024b). However, we show in Section 5 that our results are not sensitive to the choice of distribution shape.

2.3. IGM damping wing absorption

During the EoR, the damping wing absorption from the residual HI patches along the line of sight can strongly attenuate the Ly α line (c.f. the $\exp[-\tau_{IGM}]$ curve in Fig. 2). The damping wing optical depth is mostly sensitive to the distance to the nearest neutral HI patch (e.g. Miralda-Escudé 1998). Indeed, this is why we will be able to infer the size of the local HII bubble in this work (see also the complementary empirical approach in Lu et al. 2024b based on empirical $\tau_{IGM} - R_b$ relations from an EoR simulation). Nevertheless, the surrounding EoR morphology be-

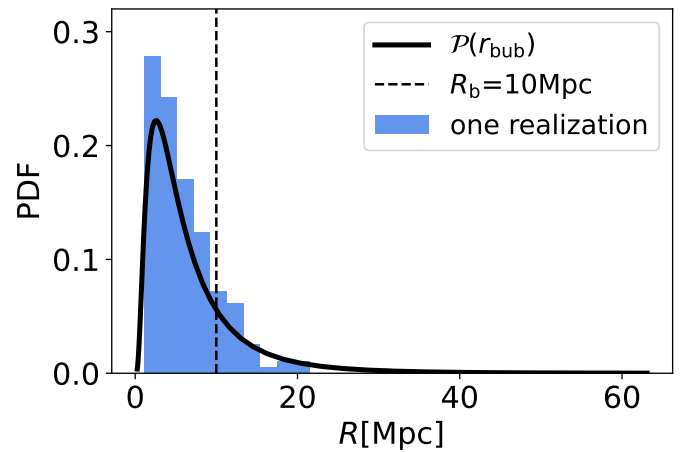


Fig. 4. Distribution of HII region radii used in our "overlapping spheres" algorithm for the large-scale EoR morphology (see text for details). The vertical dashed line marks $R_b = 10\text{Mpc}$ which is our fiducial size for the central ionized region whose properties we aim to infer (c.f. Fig. 1).

yond the local HII region does contribute to the total τ_{IGM} as an additional source of scatter (e.g. Mesinger & Furlanetto 2008a).

Here we generate an EoR morphology *at a given* \bar{x}_{HI} , by placing overlapping spherical HII regions, with a radius distribution given by (cf. Fig. 1):

$$\mathcal{P}(r_{\text{bub}}|\bar{x}_{\text{HI}}) = \frac{1}{\sqrt{2\pi}\sigma_{\text{bub}}} \cdot \exp\left(-\frac{(\log r_{\text{bub}} - \mu_{\text{bub}})^2}{\sigma_{\text{bub}}^2}\right). \quad (8)$$

We sample from the above distribution of radii, randomly choosing the center location, and stopping when the volume filling factor of ionized regions reaches the desired value, \bar{x}_{HI} . Although simplistic, overlapping ionized spheres does result in a similar EoR morphology as is seen in cosmological radiative transfer simulations (e.g. Zahn et al. 2011; Mesinger et al. 2011; Ghara et al. 2018; Doussot & Semelin 2022). We do not assume we know the true value $\bar{x}_{HI}^{\text{true}}$ a priori; instead, we sample a prior distribution of \bar{x}_{HI} from complimentary observations while performing inference (see Section 3 for more details).

For simplicity, in this proof-of-concept work we ignore the \bar{x}_{HI} dependence of the bubble size distribution in eq. (8), taking constant values of $\mu_{\text{bub}} = \log(5\text{cMpc})$ and $\sigma_{\text{bub}} = 0.5$. These choices in our algorithm roughly reproduce the ionized bubble scales seen in simulations during the early stages of the EoR (e.g., Mesinger & Furlanetto 2007; Giri et al. 2018; Lu et al. 2024b; Doussot & Semelin 2022; Neyer et al. 2024). Note that the r_{bub} from Eq. 8 does not directly translate to any of the metrics commonly used to characterize EoR morphology (e.g. Lin et al. 2016; Giri et al. 2018) and so comparisons must be done a-posteriori. In future work, we will calibrate Eq. (8) to EoR simulations, conditioning also on the matter field to account for the (modest) bias of HII regions at early times (e.g. Fig. 12 in Sobacchi & Mesinger 2014). We show our assumed bubble size distribution in Fig. 4, as well as one realization in a $200 \times 80 \times 80 \text{cMpc}^3$ volume.

For a given realization of EoR morphology and galaxy field (c.f. Fig. 1), we compute the damping wing optical depth by casting rays from the galaxy locations and summing the optical depth contributions from all HI patches along the LOS (e.g. Miralda-Escudé 1998):

$$\tau_{\text{EoR}}(\lambda_{\text{em}}) = \frac{\tau_{\text{GP}} R_{\alpha}}{\pi} \sum_i x_{\text{H},i} \left(\frac{1+z_{b,i}}{1+z_{\lambda}}\right)^{3/2} \left[I\left(\frac{1+z_{b,i}}{1+z_{\lambda}}\right) - I\left(\frac{1+z_{e,i}}{1+z_{\lambda}}\right) \right]$$

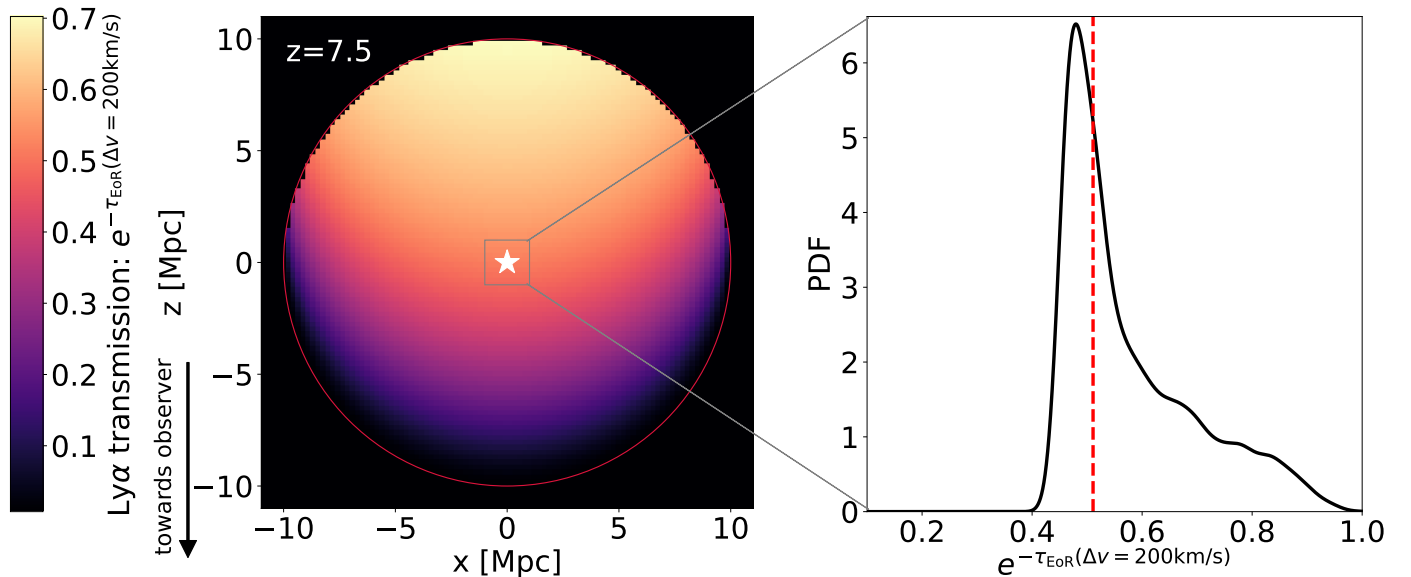


Fig. 5. *Left panel:* The *mean* Ly α transmission evaluated at $\Delta v = +200$ km/s ($e^{-\tau_{\text{EoR}}(\Delta v = +200)}$) as a function of the position inside an ionized bubble. The observer is located towards the bottom of the figure. We compute the mean transmission by averaging over 10000 realizations of EoR morphologies, given an assumed neutral fraction of $\bar{x}_{\text{HI}} = 0.65$ at $z = 7.5$ (see text for details). *Right panel:* The *distribution* of Ly α transmission at $\Delta v = +200$ km/s from these realizations, evaluated at a fixed position inside the bubble denoted by the white star (see text for details). The mean is marked by the vertical dashed line.

(9)

where $z_{\lambda} = \frac{\lambda_{\text{em}}}{\lambda_{\alpha}}(1 + z_{\text{obs}}) - 1$, λ_{em} is the wavelength at which we evaluate the optical depth, $\lambda_{\alpha} = 1215.67 \text{ \AA}$ is the Lyman-alpha resonant wavelength and z_{obs} is the redshift of the emitting galaxy. $\tau_{\text{GP}} \approx 7.16 \cdot 10^5 \left(\frac{1 + z_{\text{obs}}}{10}\right)^{3/2}$ is the Gunn-Peterson optical depth, $R_{\alpha} = \frac{\Lambda}{4\pi\nu_{\alpha}}$, $\Lambda = 6.25 \cdot 10^8 \text{ s}^{-1}$ is the decay constant and $\nu_{\lambda} = 2.47 \cdot 10^{15} \text{ Hz}$ is the Lyman- α resonant frequency. In the above equation, $I(x)$ is given by:

$$I(x) \equiv \frac{x^{9/2}}{1+x} + \frac{9}{7}x^{7/2} + \frac{9}{5}x^{5/2} + 3x^{3/2} + 9x^{1/2} - \ln \left| \frac{1+x^{1/2}}{1-x^{1/2}} \right| \quad (10)$$

The summation accounts for every neutral patch encountered along the LOS, with a given patch, i , extending from $z_{b,i}$ to $z_{e,i}$. We assume that ionized patches have no neutral hydrogen atoms so they do not contribute to the attenuation.

In the left panel of Fig 5 we show the *mean* IGM transmission, evaluated at $\Delta v = +200$ km/s redward of the systemic redshift, as a function of position inside the central HII bubble of $R_b = 10$ cMpc. The observer is located towards the bottom of the figure. This mean transmission was computed by averaging over 10000 realizations of EoR morphologies outside the central bubble, assuming $\bar{x}_{\text{HI}} = 0.65$ (e.g. one such realization is shown in Fig. 1). As expected, there is a clear trend of increased transmission for galaxies located at the far end of the central HII bubble. The mean transmission is a function of the distance of the galaxy to the bubble edge in the direction towards the observer. In Lu et al. 2024b we used these trends to define empirical "edge detection" algorithms.

However, at every location in the bubble, there is sizable sightline-to-sightline scatter in the IGM transmission. We quantify this in the right panel of Fig. 5, showing the transmission PDF constructed from the 10000 realizations of EoR morphology external to the central bubble. The sightlines used to compute this PDF originated from the location marked by the white star in the left panel. The PDF is quite broad and asymmetric

(see also Fig. 2 in Mesinger & Furlanetto 2008b as well as Lu et al. 2024a). While it is difficult for the IGM to completely attenuate Ly α for a galaxy located at the center of this bubble, some morphologies can result in large stretches of ionized IGM in the direction of the observer, driving a high-transmission tail in the PDF. The width of this PDF highlights the importance of accounting for stochasticity in the EoR morphology when interpreting galaxy Lyman alpha observations (e.g. Mesinger & Furlanetto 2008a; Mesinger et al. 2015; Mason et al. 2018; Brunt et al. 2023; Keating et al. 2024; Lu et al. 2024b).

2.4. Including NIRSpect noise

We take NIRSpect on JWST for our fiducial spectrograph in this work, which is already measuring Ly α spectra from galaxy groups during the EoR (e.g. Tang et al. 2024a; Witstok et al. 2024a). To forward-model NIRSpect observations, we bin the observed flux $f_{\alpha}(\lambda) = L_{\alpha} J(\lambda) e^{-\tau_{\text{EoR}}(\lambda)}$ to $R \sim 2700$ (high-resolution of NIRSpect), then add Gaussian noise \mathcal{N} to each spectral bin, with a standard deviation of $\sigma(\mathcal{N}) = 2 \times 10^{-20} \text{ ergs}^{-1} \text{ cm}^{-2} \text{ \AA}^{-1}$. This level of noise is obtainable with roughly a few hours of integration on NIRSpect (Bunker et al. 2023; Saxena et al. 2023; Tang et al. 2024a), and corresponds to an uncertainty on the integrated flux ($\mathcal{F}_{\text{int}} \equiv \int f_{\alpha}(\lambda) d\lambda$) of $\sigma(\mathcal{N}_{\text{int}}) = 1 \times 10^{-19} \text{ ergs}^{-1} \text{ cm}^{-2}$ (estimated assuming the emission line is spectrally unresolved). This can be further translated to 5σ limiting equivalent widths of $W = 25 \text{ \AA}$ ($W = 60 \text{ \AA}$) for $M_{\text{UV}} = -18$ ($M_{\text{UV}} = -17$). We also find worse recovery assuming shallower observations, while our results do not improve significantly assuming deeper integrations than this fiducial value.

We re-bin the spectra to lower values of R and test the inference with a coarser resolution. By performing additional binning, we lose some information on the observed line profile (e.g. Byrohl & Gronke 2020), but lower the dimensionality of our likelihood (see Section 3). In future work, we will explore more sophisticated inference approaches that can scale to high-

dimensional likelihoods (Cranmer et al. 2020; Anau Montel et al. 2024). Here we empirically settle on rest-frame $\Delta\lambda \sim 1\text{\AA}$ as our bin width (i.e. $R \sim 1000$), corresponding to the medium resolution NIRSspec grating (Jakobsen et al. 2022, see Section 3).

3. Inferring the local HII bubble

With the above framework, we can create mock observations and corresponding forward models by sampling each of the terms in Eq. 2. We detail this procedure below.

3.1. Mock observations

We first construct a mock observation of N_{gal} galaxies in a survey volume of $V_{\text{survey}} = 20 \times 20 \times 20 \text{ cMpc}^3$ ($\sim 7' \times 7' \times \Delta z = 0.07$) at $z = 7.5$. This FoV is roughly motivated by *JWST* (corresponding to roughly 4 NIRSspec pointings), though in practice the forward-modeled volume should be tailored to the specific observation that is being interpreted. We place a bubble with radius $R_b = 10 \text{ cMpc}$ at the (arbitrarily-chosen) center of the volume, and construct the surrounding EoR morphology out to distances of 200 cMpc^2 , using the prescription from Sect. 2.3 and assuming $\bar{x}_{\text{HI}} = 0.65$. Below we demonstrate that our results are insensitive to these fiducial choices.

We assign random locations to the galaxies, \mathbf{x}^i with $i \in [1, N_{\text{gal}}]$, using rejection sampling to ensure that on average 75% of the galaxies are inside HII regions (roughly matching results from simulations; e.g. Lu et al. 2024a). This is a very approximate way of accounting for galaxy bias, as both galaxies and HII regions are correlated to the large-scale matter field.³

We generate UV magnitudes for each galaxy by sampling the UV luminosity function (LF) from Park et al. (2019) down to a magnitude limit of $M_{\text{UV}} = -18.0$. Each galaxy is then assigned an emergent emission profile according to the procedure in the previous section, which is attenuated by its sightline through the realization of the EoR morphology. Finally, a noise realization is added to the binned flux to create a mock spectrum for each galaxy (c.f. Eq. 2).

3.2. Maximum likelihood estimate of bubble size and location

We then interpret this mock observation by forward modeling the observed flux for each galaxy, varying: (i) the position and radius of the central HII bubble; (ii) the surrounding EoR morphology; (iii) the neutral fraction of the Universe (within ± 0.1 of the "truth", conservatively wider than current limits Qin et al. 2024); (iv) the emergent Lyman alpha flux given the galaxy's observed M_{UV} (i.e. W and v_α); (v) NIRSspec noise realizations.

For each forward model, we compute the likelihood of the mock observation, given the location and radius of the central HII region. Our sampling procedure effectively marginalizes over the unknowns (ii) – (v) from above. Because mapping out the joint likelihood over all of the observed galaxies would be

² Neutral IGM at larger distances contributes a negligible amount to the total attenuation, due to the steepness of the damping wing profile (Mesinger & Furlanetto 2008a).

³ This is a reasonable approximation, as evidenced by our results in Section 5.2, where we apply our framework to simulations that self-consistently account for galaxy and HII region bias. Indeed, observations of galaxies demonstrate that the bias dominates clustering at larger scales (\gtrsim tens of cMpc), while the smaller scales relevant for this work are dominated by Poisson noise (Bhowmick et al. 2018; Kragh Jespersen et al. 2024, Davies et al. in prep).

numerically challenging, we make the simplifying assumption that the likelihood of the observed flux from each galaxy, $f_\alpha^i(\lambda)$, is independent from the other galaxies. This allows us to write the total likelihood of the observation as a product of the likelihoods of the individual galaxies:

$$\mathcal{L} = \prod_i^{N_{\text{gal}}} \mathcal{L}^i(f_\alpha^i(\lambda) | O_b, R_b, \mathbf{x}^i, M_{\text{UV}}^i, z) \quad (11)$$

While this assumption is clearly incorrect, here we present results only in terms of the maximum likelihood, $\hat{\mathcal{L}}$. We demonstrate below that Eq. (11) provides an unbiased estimate of $\hat{\mathcal{L}}$.⁴

It is important to note that *we do not assume a Gaussian likelihood for the observed flux at each wavelength*, as is commonly done. With high S/N spectra, correlations between flux bins can be significant. Instead we directly map out the *joint PDF of flux over all wavelength bins*, $\mathcal{L}^i(f_\alpha^i(\lambda_1), f_\alpha^i(\lambda_2), f_\alpha^i(\lambda_3), \dots | O_b, R_b, \mathbf{x}^i, M_{\text{UV}}^i, z)$, using kernel density estimation over the forward-modeled spectra (see Appendix A for details). This preserves the covariances between the wavelength bins, and is commonly known as implicit likelihood or simulation based inference.

We demonstrate this procedure for the three galaxies shown in Fig. 1. The observed flux from galaxies 'A', 'B', and 'C', is denoted in gray in the three panels of Fig. 6, left to right respectively. In blue we show the 68% C.L. of the likelihood assuming the correct HII bubble location and radius, $(R_b, O_b) = (R_b^{\text{true}}, O_b^{\text{true}})$. In red we show the 68% C.L. of the flux likelihood assuming the correct HII bubble location but a slightly smaller radius, $R_b = 0.8R_b^{\text{true}}$. Galaxy 'A' in this mock observation is outside of the central HII bubble, and therefore the true and slightly smaller values of R_b result in the same likelihood. Galaxy 'B' is located close to the center of the bubble, so both $R_b = R_b^{\text{true}}$ and $R_b = 0.8R_b^{\text{true}}$ give similar values of transmission $\exp[-\tau_{\text{EoR}}]$ (see Fig. 5). This results in only a slight preference for $R_b = R_b^{\text{true}}$. On the other hand, galaxy 'C' is located close to the edge of the bubble in Fig. 1. For that galaxy, we see that the observed spectrum in gray is more consistent with the correct likelihood in blue than with the incorrect one in red. Having a smaller bubble would imply more IGM attenuation on average at the location of this galaxy, making the observed strong Ly α emission less likely. In this specific realization, the joint likelihood (Eq. 11) of the observed fluxes of 'A', 'B', and 'C' is two times larger for the correct value of bubble radius than for the incorrect one. As one includes more and more galaxies, the maximum likelihood becomes increasingly peaked around the true values for the bubble size and location.

We illustrate this explicitly in Figure 7, in which we plot 2D slices through the log likelihood. The log likelihood normalized to the maximum value is indicated with the color bar. The vertical and horizontal axis in each panel correspond to the sampled bubble radius, R_b , and redshift axis of the center, $O_b = (x_b = x_b^{\text{true}}, y_b = y_b^{\text{true}}, z_b)$. The true values, $(R_b^{\text{true}}, z_b^{\text{true}}) = (10 \text{ cMpc}, 0 \text{ cMpc})$, are demarcated with the dashed lines. The columns correspond to increasing number density of observed

⁴ Ideally, we would want to map out the full posterior:

$$\mathcal{P}(O_b, R_b | \mathbf{x}, f_\alpha(\lambda), M_{\text{UV}}, z) \propto \mathcal{L}(f_\alpha(\lambda) | O_b, R_b, \mathbf{x}, M_{\text{UV}}, z) \pi(O_b, R_b),$$

where $\pi(O_b, R_b)$ is a prior for the center location and radius of the HII bubble. However, including the correlations of the (non-Gaussian) likelihoods at the location of every galaxy is analytically not tractable, and would require high dimensional simulation based inference (e.g., de Santi et al. 2023; Lemos et al. 2023). We save this for future work.

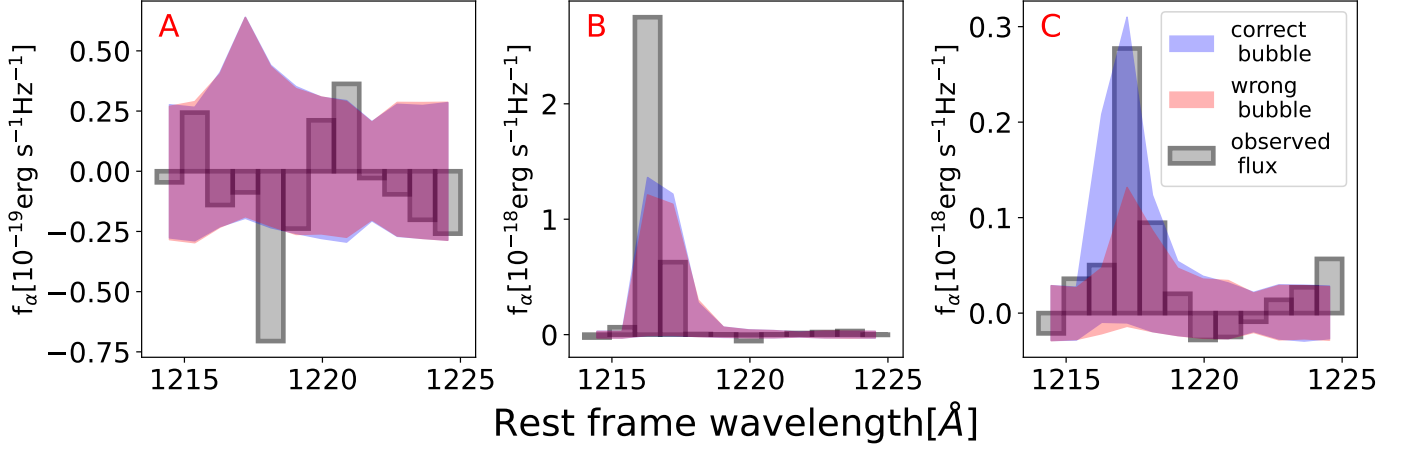


Fig. 6. The observed flux (*gray*) corresponding to the galaxies 'A', 'B', and 'C' from the mock observation shown in Fig. 1. In blue we show the 68% C.L. of the likelihood assuming the correct HII bubble location and radius, $(R_b, O_b) = (R_b^{\text{true}}, O_b^{\text{true}})$. In red we show the 68% C.L. of the flux likelihood assuming the correct HII bubble location but a slightly smaller radius, $R_b = 0.8R_b^{\text{true}}$. We see that the observed flux is more consistent with the blue likelihood than the red likelihood, mostly due to galaxy 'C' that is located close to the edge of the bubble (note the different y-axis ranges in each panel, with the observed flux from galaxy 'A' being noise dominated).

galaxies (*left to right*), while rows correspond to different realizations of forward models.

There are several interesting trends evident in Figure 7. Firstly, we see that increasing the number of observed galaxies (going from left to right in each row) results in an increasingly peaked likelihood, with the maximum settling on the true values for the bubble radius and location. Different realizations of the EoR morphology give different likelihood distributions when a small number of galaxies is observed. However, as the number density of observed galaxies is increased, the likelihood distributions between different realizations converge (i.e. all sources of stochasticity are "averaged out").

We also see a degeneracy between the redshift of the bubble center and its radius. Because the transmission is mostly determined by the distance to the bubble edge along the line of sight, moving the bubble center further away from the observer at a fixed radius is roughly degenerate with decreasing the radius at a fixed center location. This degeneracy is mitigated by having a larger number of sightlines to observed galaxies, allowing us to constrain the radius of curvature of the bubble.

4. How many galaxies do we need to confidently infer the local HII bubble?

In the previous section, we demonstrated that our framework gives an unbiased estimate of the HII region size and location when applied to a large galaxy sample. Here we quantify just how "large" does this galaxy sample need to be, in order for us to be confident in our results. For this purpose we define two figures of merit:

$$\text{Err}_{\text{loc}} = \left| \hat{O}_b(n_{\text{gal}}) - O_b^{\text{true}} \right| / R_b^{\text{true}} \quad (12)$$

$$= \sqrt{(\hat{x}_b - x_b^{\text{true}})^2 + (\hat{y}_b - y_b^{\text{true}})^2 + (\hat{z}_b - z_b^{\text{true}})^2} / R_b^{\text{true}}$$

$$\text{Err}_{\text{rad}} = \left| \hat{R}_b(n_{\text{gal}}) - R_b^{\text{true}} \right| / R_b^{\text{true}}. \quad (13)$$

Here, $\hat{O}_b(n_{\text{gal}})$ and $\hat{R}_b(n_{\text{gal}})$ are the maximum likelihood estimates of the HII bubble center and radius computed from a galaxy field with number density $n_{\text{gal}} = N_{\text{gal}}/V_{\text{survey}}$, and Err_{loc}

and Err_{rad} are the corresponding fractional errors (normalized to the true bubble radius).

Since we are calculating the likelihood on the grid, we can say that our framework "has found" the optimal bubble when the fiducial and inferred locations and radii coincide, i.e. $\text{Err}_{\text{loc}} = \text{Err}_{\text{rad}} = 0$. In that case, the error of location and radius is below the grid on which we calculate the likelihood (1.5cMpc in our fiducial case, corresponding to a $\lesssim 15\%$ fractional error).

The solid black curve in Fig. 8 shows how these fractional errors change with galaxy number density for a single realization. Here the realization of EoR morphology and "observed" galaxies are held constant, with the maximum likelihood computed each time a new "observed" galaxy is added. The more galaxies we observe, the smaller the error on our inferred HII bubble location and radius. The sizable stochasticity in galaxy properties and sightline-to-sightline scatter in the IGM opacity manifest as "noise" in this evolution, making it non-monotonic. Nevertheless, even a single galaxy is able to shrink the fractional error by a factor of two from our prior range, ruling out extreme values.

We repeat this calculation with 100 different realizations of the mock observation (EoR morphology and observed galaxy samples). In Fig. 8 we show the resulting 68% and 95% C.L. on the fractional errors as more and more galaxies are added to the field. We see that in 68% (95%) of cases, number densities of $7.7 \times (10.5 \times) 10^{-3} \text{cMpc}^{-3}$ are sufficient to obtain a $\lesssim 15\%$ error on the center position. The corresponding requirements are $4.2 \times (7.2 \times) 10^{-3} \text{cMpc}^{-3}$ for $\lesssim 15\%$ error on the bubble radius (comparable to Lu et al. 2024b). In other words, Ly α spectra from ~ 0.01 galaxies per cMpc^3 are required to be $\geq 95\%$ confident that the HII bubble location and size recovered by our method is accurate at $\lesssim 1$ cMpc. This corresponds roughly to 80 galaxies in 2x2 tiled pointings with JWST/NIRSpec.

4.1. Including a prior on the emergent Lyman alpha

In this work we assume the emergent Lyman alpha emission follows post-EoR empirical relations, as described in Section 2.1. Beyond this, we assume no prior knowledge on each galaxy's intrinsic emission. However, lower opacity nebular lines such as the Balmer lines ($H\alpha$, $H\beta$), can provide complimentary estimates of the intrinsic production of Lyman alpha photons (e.g. Hayes

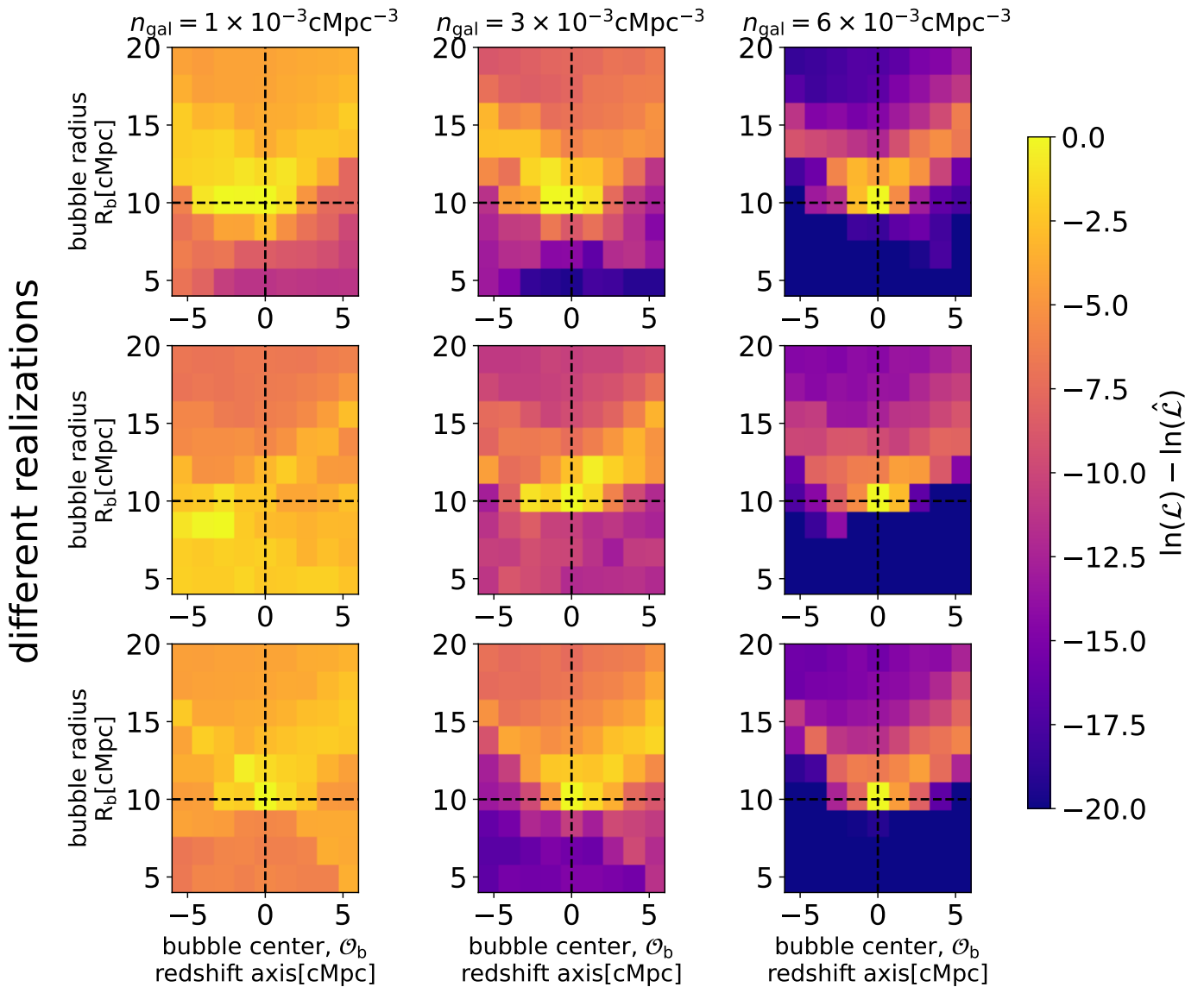


Fig. 7. 2D slices through the log likelihood, normalized to the maximum value in each panel. The vertical and horizontal axis in each panel correspond to the bubble radius, R_b , and redshift axis of the center, $\mathcal{O}_b = (x_b = x_b^{\text{true}}, y_b = y_b^{\text{true}}, z_b)$. The true values, $(R_b^{\text{true}}, z_b^{\text{true}}) = (10 \text{ cMpc}, 0 \text{ cMpc})$, are demarcated with the dashed lines. The mock observation in this example was made at $z = 7.5$, assuming $\bar{x}_H = 0.65$. Different columns represent different numbers of galaxies used for inference (8 on the left, 24 in the middle and 48 on the right). Different rows correspond to different realizations of EoR morphology and galaxy samples.

et al. 2023; Saxena et al. 2023; Chen et al. 2024). In this section we repeat the analysis from above, but including a simple prior on the emergent Ly α emission.

Specifically, we apply rejection sampling to keep only those forward-models for which the transmission is within 20% of the true one (or putting an upper bound if $\mathcal{T}_{\text{EoR}} \leq 0.2$)⁵ Then we calculate the likelihood the same way as we did in Section 3. The width of the prior is motivated by current observations us-

⁵ A detection of Balmer lines puts constraints on the production rate of Lyman alpha photons, who then have to pass through the ISM, CGM and IGM. Our distribution of Lyman- α equivalent widths and profile shapes described in Section 2.2 effectively already includes radiative transfer and escape through the ISM + CGM, which we assume does not evolve significantly with redshift at $z \gtrsim 6$. Thus our prior is effectively a prior on the IGM transmission. We leave a self-consistent treatment of the redshift evolution of ISM+CGM escape fraction and IGM transmission for future work.

ing JWST (c.f. Saxena et al. 2023 for H β , and Lin et al. 2024 for H α from ground instruments). Note that H α observations above $z > 7$ are not possible with NIRSpec. For higher redshifts, we therefore have to rely on a fainter H β . Despite this, H β is regularly observed in high- z galaxies, so using the prior for all galaxies is not unreasonable (e.g., Meyer et al. 2024).

In Fig. 9 we show the 95% C.L. on the fractional errors with (red) and without (blue; same as Fig. 8) the prior information on the emergent Lyman alpha emission. We see that using additional nebular lines to constrain the emergent Lyman alpha emission can reduce by a factor of ~ 2 the required number of galaxies to obtain the same constraints.

4.2. Results for different bubble sizes

Our fiducial choice for the radius of the central HII bubble is $R_b = 10 \text{ Mpc}$, motivated by HII bubble sizes in the early stages

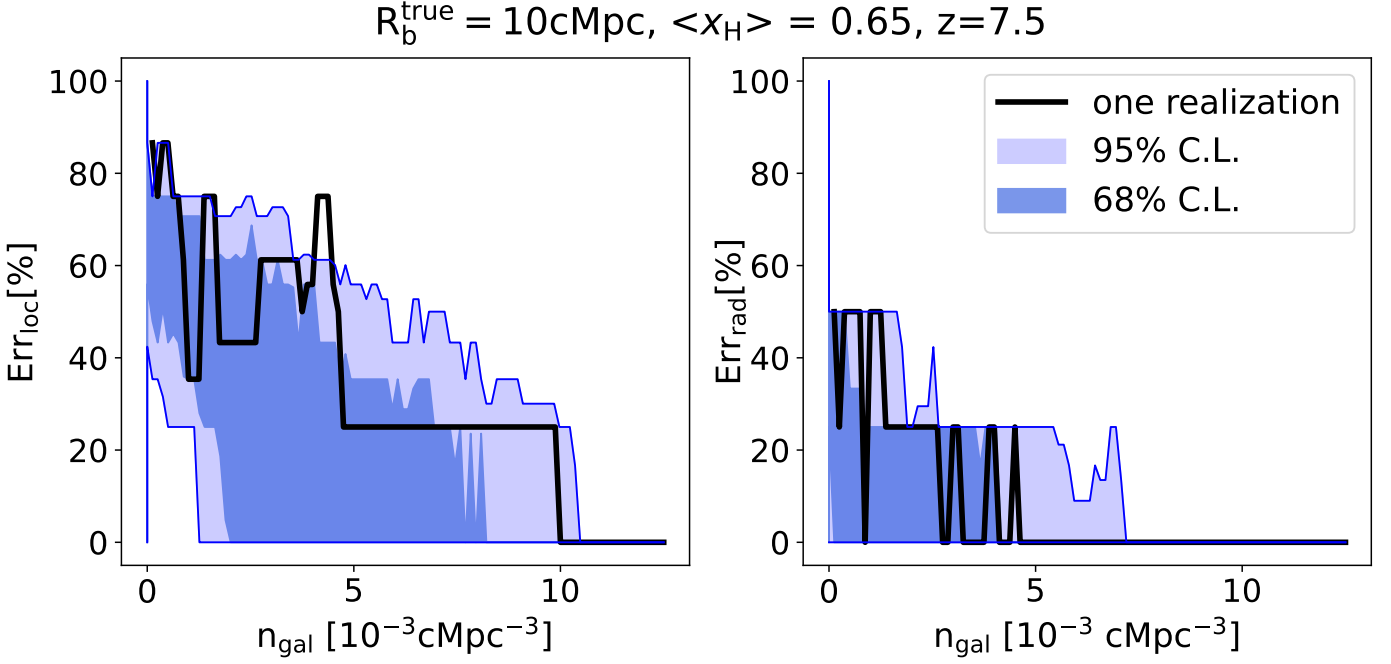


Fig. 8. Fractional errors of the maximum likelihood HII bubble center (*left*) and radius (*right*) as a function of the number density of observed galaxies. The black curve corresponds to a single realization of the EoR morphology and galaxy samples. The light (dark) blue region corresponds to the 95th (68th) percentile of fractional errors obtained from 100 realizations. With $n_{\text{gal}} \gtrsim 0.01$ galaxies cMpc^{-3} , the fractional errors drop below the grid resolution we use to calculate the likelihoods (1.5cMpc).

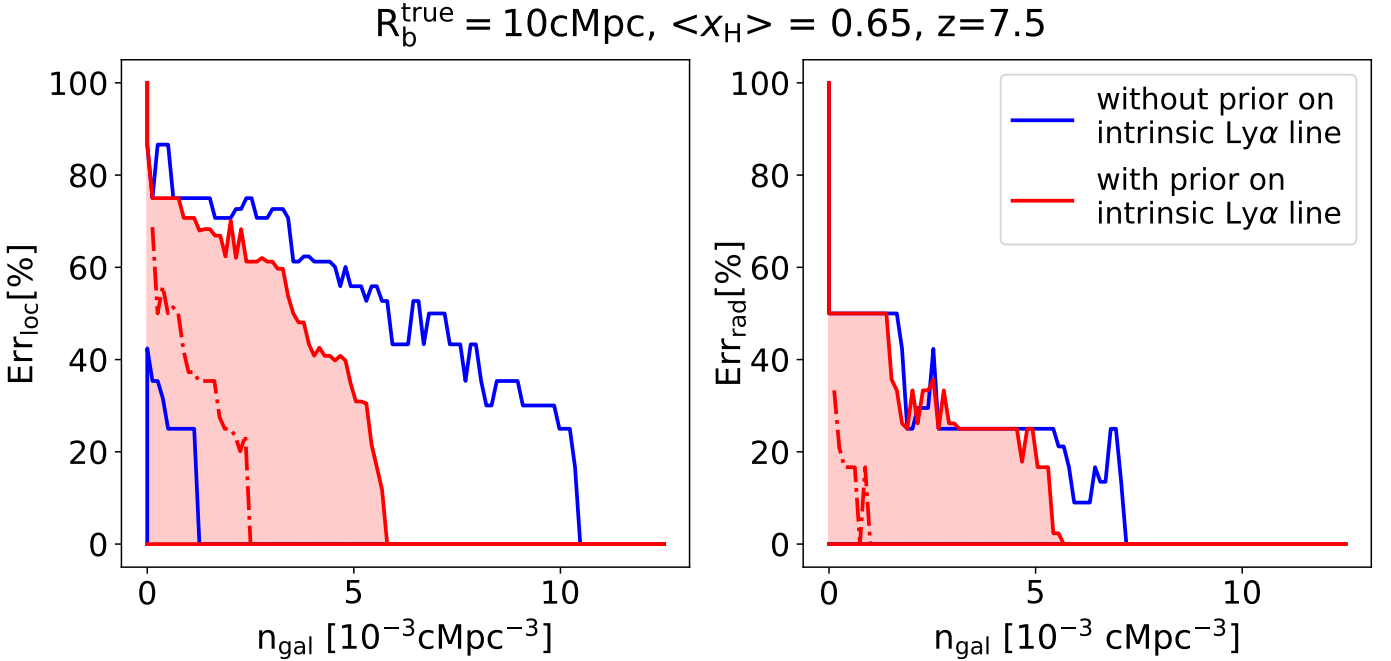


Fig. 9. Same as Fig. 8, but we include in red the 95% C.L. on the fractional errors assuming a prior on the emergent Lyman alpha emission, motivated by observed Balmer lines (see text for details). Compared to the analogous results without including a prior (*blue*), we see that the required number of galaxies to achieve the same accuracy is reduced by roughly a factor of two.

of the EoR. Here we test the performance of our pipeline for other radii, $R_b = 5$ and 15Mpc .

In the top (bottom) panels of Fig. 10 we show the analysis with and without the 20% prior on the emergent emission, assuming $R_b^{\text{true}} = 5\text{Mpc}$ ($R_b^{\text{true}} = 15\text{Mpc}$). Comparing to the fiducial results in Fig. 9, we see that fewer galaxies are required to

infer the size and location for larger HII bubbles. For $R_b^{\text{true}} = 15\text{cMpc}$ roughly 2-3 times fewer galaxies are required to constrain the HII bubble with the same accuracy, compared to $R_b^{\text{true}} = 5\text{cMpc}$. This is most likely due to the fact that the larger bubbles allow for a broader range of IGM opacities. Galaxies inside small bubbles have roughly the same attenuation regardless of

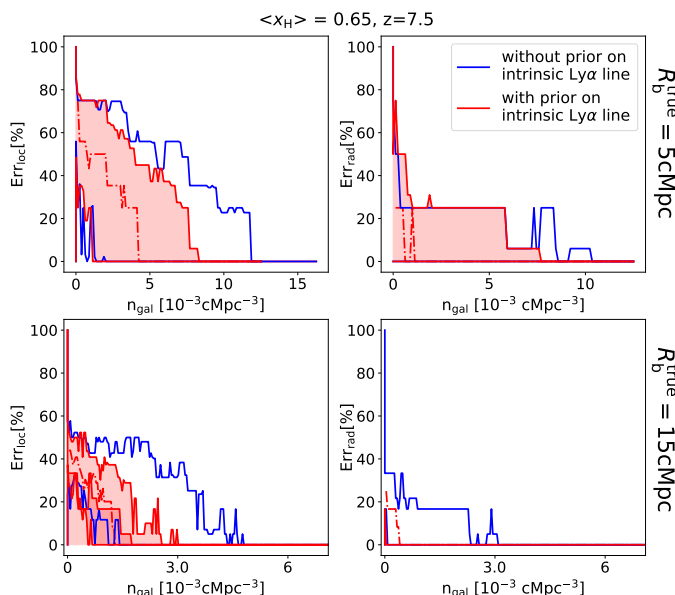


Fig. 10. Same as Fig. 9, but assuming $R_b^{\text{true}} = 5$ (15) cMpc in the top (bottom) row. Larger bubbles can be inferred with the same accuracy using a smaller number density of galaxies.

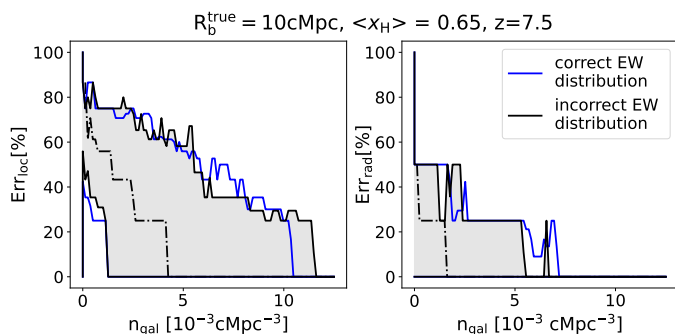


Fig. 11. Same as Fig. 8, but including in gray the 95% C.L. on the fractional errors assuming that the EW distribution we use to interpret the mock observation is incorrect. In other words, the mock observations and forward models are generated using different EW distributions (see text for details). The fact that the C.L. demarcated in gray and blue roughly overlap indicates that our results are not sensitive to our choice of the emergent EW distribution.

their relative location inside the bubble. In contrast, for larger bubbles there is a noticeable difference between the (average) attenuation on the near side and far of the bubble, allowing us to more easily constrain their geometry (c.f. the left panel of Fig. 5).

5. Building confidence in our framework

In this section, we explore how do our results depend on our model assumptions. To do this, we apply our framework on a different reionization morphology and on different emergent EW distributions. Even though our framework is a proof-of-concept, having it perform well on such "out-of-distribution" tests would help build confidence that it is not sensitive to uncertainties in the details of our model.

5.1. Different EW distribution

First, we test the performance of our pipeline assuming the emergent Lyman- α luminosities follow a different EW distribution than the we use in our forward-models (Sec. 2.2). Specifically, we generate mock observations assuming a Gaussian distribution from [Treu et al. \(2012\)](#) (based on [Stark et al. \(2011\)](#)), but with the same parameters as in Section 2.2):

$$p_{6;G}(W|M_{UV}) = \frac{A(M_{UV})}{W_c(M_{UV})} \sqrt{\frac{2}{\pi}} e^{-\frac{1}{2}\left(\frac{W}{W_c(M_{UV})}\right)^2} H(W) + [1 - A(M_{UV})]\delta(W) \quad (14)$$

We then interpret these mock observations with our fiducial pipeline, which uses the exponential EW distribution from Eq. 7.

The resulting 95% C.L. on the fractional errors are highlighted in gray in Fig. 11. In blue, we show the same 95% C.L. from Fig. 8, which use same EW distribution for the forward models and the mock observation. The fact that the gray and blue regions demarcate roughly the same fractional errors suggests that our analysis is not sensitive to the choice of EW distribution.

5.2. Demonstration on a 3D reionization simulation

Because this work is intended as a proof-of-concept, throughout we made several simplifying assumptions. For example, our reionization morphology is generated by overlapping ionized spheres and we have only a simplified treatment for galaxy – HII bubble bias. Including a more realistic bias for both galaxies and HII regions would be straightforward to do analytically, but it is necessary? Here we test how our simple model performs on self-consistent 3D simulations of reionization.

We apply our framework on the galaxy catalogs and ionization maps from the simulations of [Lu et al. \(2024b\)](#), generated with the public 21cmFAST code ([Mesinger & Furlanetto 2007](#); [Mesinger et al. 2011](#); [Murray et al. 2020](#)). These simulations capture the complex morphology of reionization, which is self-consistently generated from the underlying galaxy fields. We process the galaxies with the procedure outlined in Section 2 to create mocks on which we can perform the inference.

We use two ionization boxes, one at $\bar{x}_{\text{HI}} = 0.69$ and $\bar{x}_{\text{HI}} = 0.90$. We select ionized bubbles and associated galaxies that match the volumes we use in our fiducial set-up, specifically $20 \times 20 \times 20$ cMpc. When applying the inference framework to real data, one should of course tailor the forward models to match the specific details of the survey.

We illustrate the results in Figures 12 and 13, for a couple of example surveys at $\bar{x}_{\text{HI}} = 0.69$ and $\bar{x}_{\text{HI}} = 0.9$, respectively. In the left panels, we show 1.5 cMpc thick slices through the simulation boxes. Ionized/neutral regions are shown as white/black. The brightest galaxies are shown with stars, whose colors correspond to their UV magnitudes. The line of sight direction used to compute the IGM opacity for each observed galaxy is indicated with the arrow.

The volumes of the mock surveys are illustrated with the zoom-ins on the right. Here, gray cells show the ionized voxels of the simulation, and the blue sphere is the maximum likelihood solution for the central HII region. We assumed all galaxies inside this $20 \times 20 \times 20$ cMpc volume brighter than $M_{UV} < -17.0$ are observed with NIRSpect. This corresponds to $\sim 50(30)$ galaxies at $\bar{x}_{\text{HI}} = 0.69$ ($\bar{x}_{\text{HI}} = 0.9$).

We see from the zoom-ins in these figures that the inferred HII regions in blue provide a reasonable characterization of the

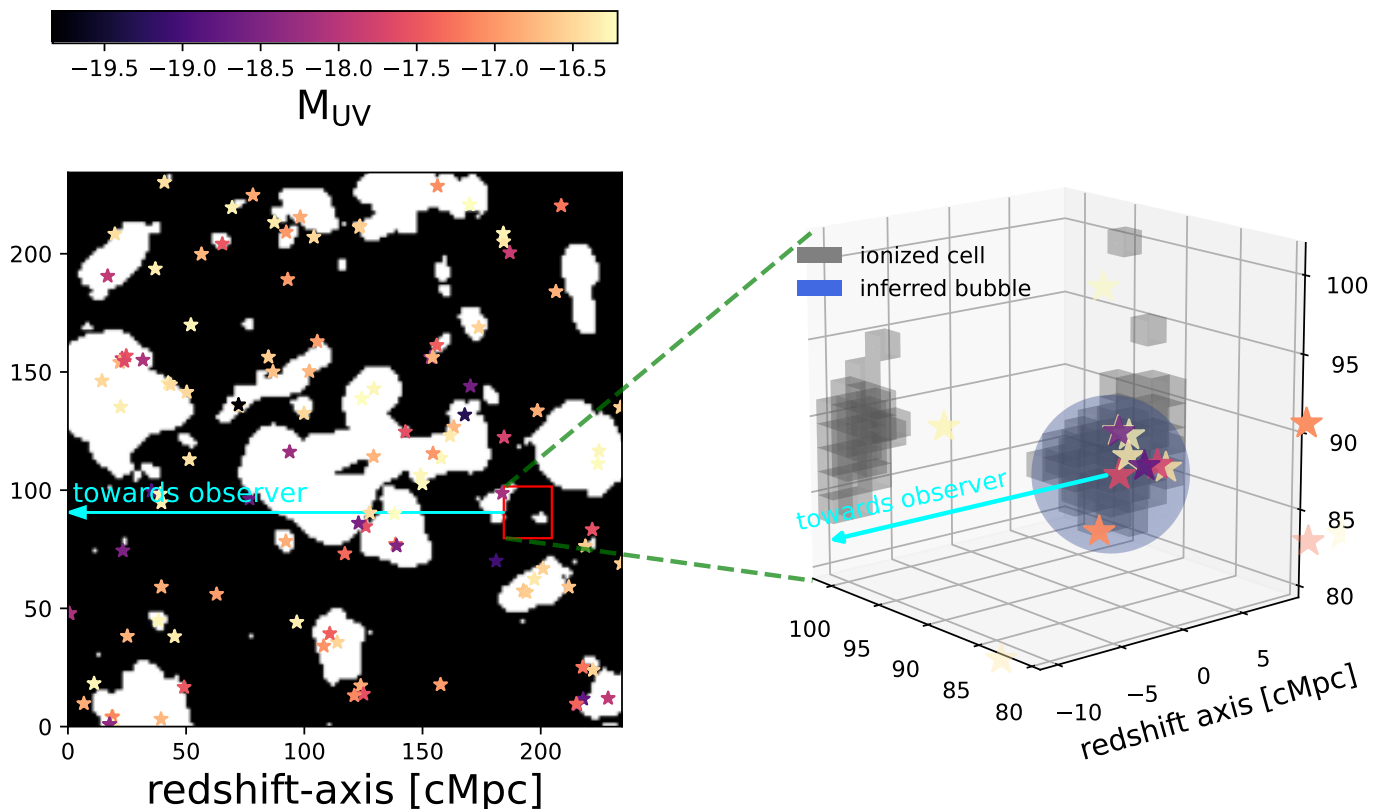


Fig. 12. Application of our bubble-finding procedure to a 3D simulation. *Left:* 2D slices through the ionization field. Ionized/neutral regions are shown as white/black. The brightest galaxies in this 1.5 cMpc slice are denoted with stars, colored according to their UV magnitudes. The line of sight direction used to compute the IGM opacity for each observed galaxy is indicated with the arrow. The 20x20x20 cMpc sub-volume used for the mock survey is denoted with the red square. *Right:* Zoom-in of the mock survey. A random sub-sample (to avoid overcrowding) of the observed galaxies are shown with stars. Ionized voxels are shown in gray. Our maximum likelihood solution for the central HII bubble is overlaid with the blue sphere. The reasonable overlap of the central gray blob with the blue sphere lends confidence in our framework.

"true" HII region in gray. This gives us confidence in our simplified treatment of the EoR morphology and the associated spatial correlation with galaxies. As mentioned above, we will tailor future applications to actual NIRSpect surveys of galaxy groups.

6. JWST observational requirements

We currently have several spectroscopically-targeted fields containing groups of galaxies with detection in Lyman- α , such as COSMOS (Endsley & Stark 2022; Witten et al. 2024), EGS (Oesch et al. 2015; Zitrin et al. 2015; Roberts-Borsani et al. 2016; Tilvi et al. 2020; Leonova et al. 2022; Larson et al. 2022; Jung et al. 2022; Tang et al. 2023, 2024b; Chen et al. 2024; Napolitano et al. 2024), BDF (Castellano et al. 2016, 2018), GOODS-N (Oesch et al. 2016; Eisenstein et al. 2023; Bunker et al. 2023; Tacchella et al. 2023) and GOODS-S (Witstok et al. 2024b; Tang et al. 2024b). Although the number densities are a factor of few lower ($\sim 1.0 \times 10^{-3} \text{cMpc}^{-3}$) than the required values in Section 4, the data sets are expanding rapidly. On-going and proposed programs are extending fields and going deeper, resulting in larger areas and number densities. Here we quantify in more detail the JWST survey requirements in order to be able to robustly constrain HII bubbles with our procedure.

In Fig. 14 we show the number density of galaxies as a function of limiting UV magnitude, $M_{\text{UV}}^{\text{lim}}$ and galaxy overdensity, $n(< M_{\text{UV}}^{\text{lim}}/\bar{n}(< M_{\text{UV}}^{\text{lim}}))$. We plot three curves corresponding to $M_{\text{UV}}^{\text{lim}} = -17, -18, -19$. We demarcate in gray the required number

density for accurate HII bubble recovery we found in the previous section; the lower/upper range correspond to including/not including a prior on the emergent Ly α emission from Balmer lines (c.f. Section 4).

At the mean number density, we would require the photometric survey to detect galaxies down to $M_{\text{UV}}^{\text{lim}} \lesssim -17.0 - -17.5$. The quoted range spans what can be achieved with or without a prior on the Lyman alpha production rate from Balmer lines. In an unlensed field, obtaining such number densities would require roughly 600 hours of integration with NIRCcam on JWST (estimated based on exposure times in Morishita et al. 2024, for 4 pointings): achievable, but ambitious.

However, several current fields are known to contain overdensities. For example, COSMOS contains a 140pMpc^3 volume that is estimated to be three times overdense at $z \approx 6.8$ (Endsley & Stark 2022), while EGS is estimated to contain a 12pMpc^3 volume that is also $3\times$ overdense at $z \approx 8.7$ (Zitrin et al. 2015; Leonova et al. 2022; Larson et al. 2022; Tang et al. 2023; Chen et al. 2024; Lu et al. 2024a). Also, GOODS-S and GOODS-N contain $4\times$ and $8\times$ overdensities over volumes larger than the fiducial one used in this work ($62 \text{arcmin}^2 \times \Delta z \approx 0.2$ Tang et al. 2024b). Furthermore, one of the most distant observed LAE is also believed to be located in an overdensity (up to $24\times$ overdense at $z = 10.6$ in 2.6pMpc^3 volume; Oesch et al. 2016; Bunker et al. 2023; Tacchella et al. 2023, see also Lu et al. 2024a for other examples). Observing a field with an overdensity of three (eight) would require photometric completeness down to

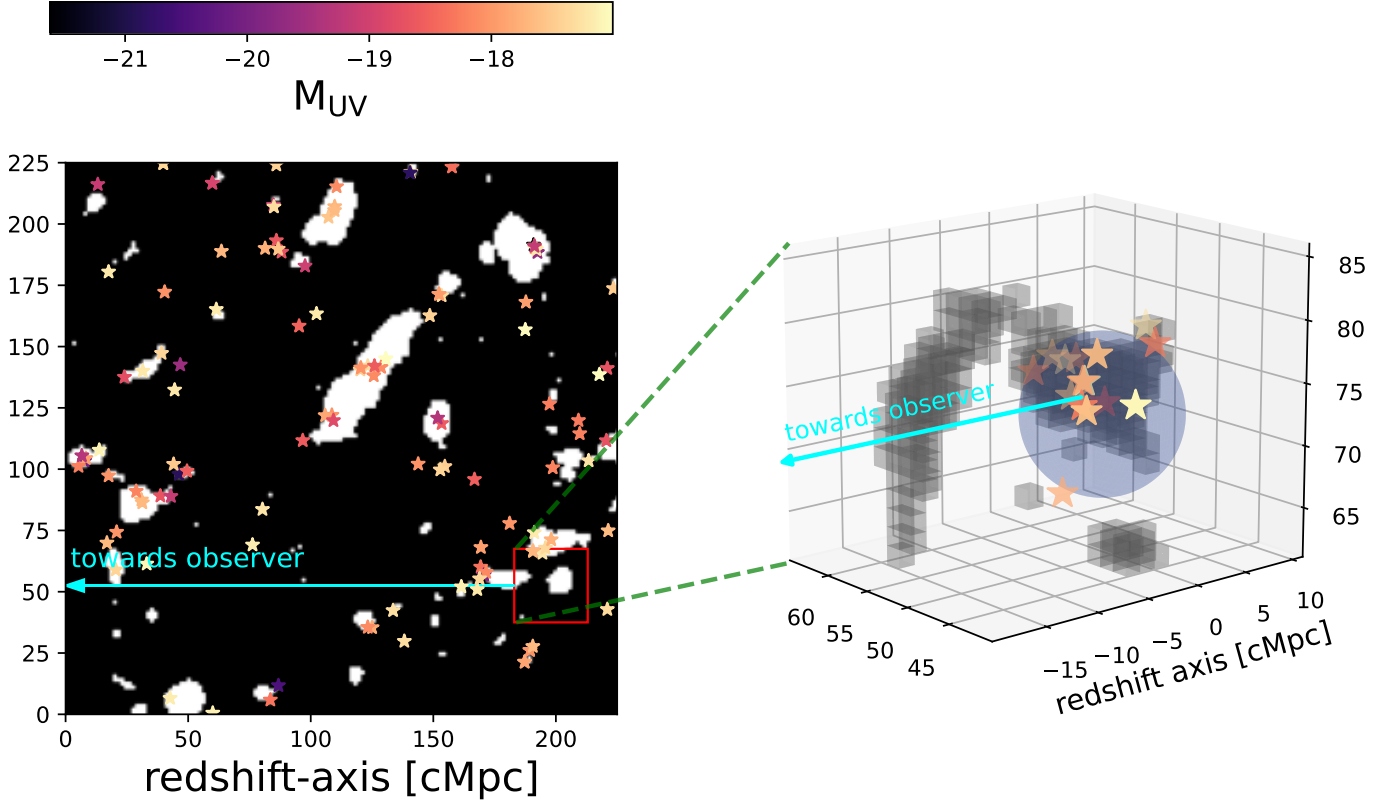


Fig. 13. The same as Fig. 12, but for $\bar{x}_{\text{HII}} = 0.9$.

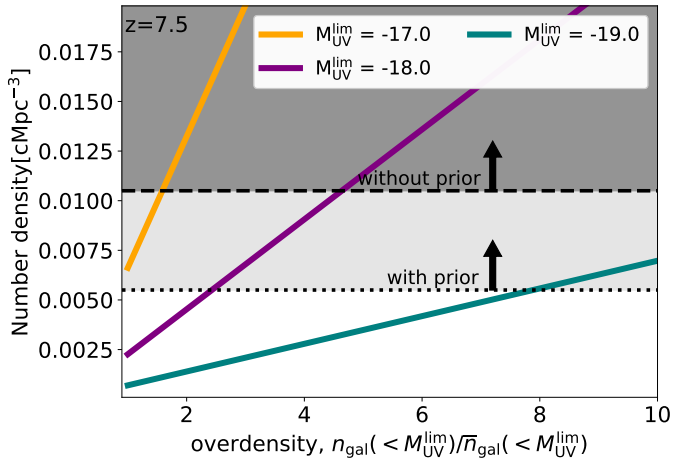


Fig. 14. Cumulative number density of galaxies down to various magnitude limits, as a function of galaxy overdensity. Dotted (dashed) lines demarcate the minimum number densities found in this work for accurate HII bubble recovery, including (not including) a prior on the emergent emission of Lyman alpha.

$M_{\text{UV}}^{\text{lim}} \lesssim -18.5 - -18$ ($-19 - -18.5$). This would require "only" 50 (4.2) hours of integration with NIRCcam.

These candidates then require spectroscopic follow-up. For spectroscopic confirmation, the best candidate is [OIII]5007Å emission line. The [OIII] emission line is routinely observed with JWST (e.g., Endsley et al. 2023, 2024; Meyer et al. 2024). We can estimate the required exposure time for detecting [OIII] line by assuming the M_{UV} dependent distribution of equivalent widths from Endsley et al. (2024). For that distribution,

the equivalent width limit for detecting 90% galaxies at $M_{\text{UV}} = -18.0$ is 120Å. Obtaining such an equivalent width (at 5σ) at $z = 7.5$ with the G395M filter requires 18 hours per pointing. The number density requirement (and thus exposure time) would increase if we do not detect H β as required to put a prior on the intrinsic Lyman- α emission. It would also increase if the [OIII] distribution is lower at lower magnitudes.

Following that, to detect Lyman α at a noise level of $5 \times 10^{-19} \text{erg s}^{-1} \text{cm}^{-2}$ (corresponding to a detection of a line of $W \approx 25\text{\AA}$) would require 23 hours with G140M per pointing. These numbers are comparable to existing large JWST surveys (Eisenstein et al. 2023).

We also note that the volume of the potential JWST surveys used for this analysis has a direct impact on the sizes of the HII regions that can be inferred (see also Lu et al. 2024b). Tiled surveys of the same depth but larger volumes, could hope to detect correspondingly-larger HII regions. The fact that larger HII regions occur later in the EoR, with a correspondingly higher galaxy number densities, might mitigate the integration time required. We postpone more systematic survey design to subsequent work in which we apply our framework to simulated 3D EoR lightcones.

Another interesting approach could be coupling the framework from Lu et al. (2024b) with the one outlined in this work. The large-scale empirical method from Lu et al. (2024b) could isolate "interesting" sub-volumes that could then be analyzed with the quantitative inference approach presented here.

7. Conclusions

The morphology of reionization tells us which galaxies dominated the epoch of cosmic reionization. Individual bubbles sur-

rounding groups of galaxies encode information on the contribution of unseen, faint sources and allow us to correlate the properties of bubbles and the galaxies they host.

In this work we build a framework to use Lyman- α observations from *JWST* NIRSpec to constrain ionization morphology around a group of galaxies. Our framework for the first time uses complementary information from sightlines to neighboring galaxies, and samples all important sources of stochasticity to robustly place constraints on the size and position of local HII bubbles.

We find that Ly α spectra from ~ 0.01 galaxies per cMpc³ are required to be $\geq 95\%$ confident that the HII bubble location and size recovered by our method is accurate to better than ≤ 1.5 cMpc. This corresponds roughly to 80 galaxies in 2x2 tiled pointings with *JWST*/NIRSpec. These requirements can be reduced by using additional nebular lines (for example H β) to constrain the intrinsic Lyman alpha emission. We find that a simple prior on the emergent Lyman- α emission reduces by a factor of \sim two the required number of galaxies to obtain the same constraints. Such number densities are achievable with a targeted survey with completeness down to $M_{UV} = -17 - -19$, depending on the over-density of the field.

We demonstrate that our framework is not sensitive to the assumed distribution for the emergent Lyman alpha emission. We also find accurate recovery of ionized bubbles when applied to 3D EoR simulations.

Our pipeline can be applied to existing observations of Lyman- α spectra from galaxy groups. Additionally, observational requirements for a statistical detection of local HII regions presented here can be used to design complimentary, new *JWST* surveys. Applying our framework to multiple, independent fields would allow us to constrain the *distribution* of bubble sizes, which helps us understand which galaxies reionized the Universe.

8. Data availability

The code related to the work is publicly available at [IvanNikolic21/Lyman alpha bubbles](https://github.com/IvanNikolic21/Lyman_alpha_bubbles).

Acknowledgements. We gratefully acknowledge computational resources of the Center for High Performance Computing (CHPC) at SNS. AM acknowledges support from the Italian Ministry of Universities and Research (MUR) through the PRIN project "Optimal inference from radio images of the epoch of reionization", the PNRR project "Centro Nazionale di Ricerca in High Performance Computing, Big Data e Quantum Computing". CAM and TYL acknowledge support by the VILLUM FONDEN under grant 37459. CAM acknowledges support from the Carlsberg Foundation under grant CF22-1322.

References

Almada Monter, S. & Gronke, M. 2024, *MNRAS*, 534, L7
 Anau Montel, N., Alvey, J., & Weniger, C. 2024, *MNRAS*, 530, 4107
 Bhowmick, A. K., Campbell, D., Di Matteo, T., & Feng, Y. 2018, *MNRAS*, 480, 3177
 Bolan, P., Bradáč, M., Lemaux, B. C., et al. 2024, *MNRAS*, 531, 2998
 Bolan, P., Lemaux, B. C., Mason, C., et al. 2022, *MNRAS*, 517, 3263
 Bosman, S. E. I., Davies, F. B., Becker, G. D., et al. 2022, *MNRAS*, 514, 55
 Bruton, S., Scarlata, C., Haardt, F., et al. 2023, *ApJ*, 953, 29
 Bunker, A. J., Saxena, A., Cameron, A. J., et al. 2023, *A&A*, 677, A88
 Byrohl, C. & Gronke, M. 2020, *A&A*, 642, L16
 Castellano, M., Dayal, P., Pentericci, L., et al. 2016, *ApJ*, 818, L3
 Castellano, M., Pentericci, L., Vanzella, E., et al. 2018, *ApJ*, 863, L3
 Chen, Z., Stark, D. P., Mason, C., et al. 2024, *MNRAS*, 528, 7052
 Cranmer, K., Brehmer, J., & Louppe, G. 2020, *Proceedings of the National Academy of Science*, 117, 30055
 De Barros, S., Pentericci, L., Vanzella, E., et al. 2017, *A&A*, 608, A123

de Santi, N. S. M., Villaescusa-Navarro, F., Abramo, L. R., et al. 2023, arXiv e-prints, arXiv:2310.15234
 Dijkstra, M. 2014, *PASA*, 31, e040
 Dijkstra, M., Mesinger, A., & Wyithe, J. S. B. 2011, *MNRAS*, 414, 2139
 Dijkstra, M. & Wyithe, J. S. B. 2012, *MNRAS*, 419, 3181
 Doussot, A. & Semelin, B. 2022, *A&A*, 667, A118
 Eisenstein, D. J., Willott, C., Alberts, S., et al. 2023, arXiv e-prints, arXiv:2306.02465
 Endsley, R. & Stark, D. P. 2022, *MNRAS*, 511, 6042
 Endsley, R., Stark, D. P., Whitler, L., et al. 2023, *MNRAS*, 524, 2312
 Endsley, R., Stark, D. P., Whitler, L., et al. 2024, *MNRAS*, 533, 1111
 Ghara, R., Mellema, G., Giri, S. K., et al. 2018, *MNRAS*, 476, 1741
 Giri, S. K., Mellema, G., Dixon, K. L., & Iliev, I. T. 2018, *MNRAS*, 473, 2949
 Hayes, M. J., Runnholm, A., Scarlata, C., Gronke, M., & Rivera-Thorsen, T. E. 2023, *MNRAS*, 520, 5903
 Hayes, M. J. & Scarlata, C. 2023, *ApJ*, 954, L14
 Hu, W., Martin, C. L., Gronke, M., et al. 2023, *ApJ*, 956, 39
 Hutter, A., Trebitsch, M., Dayal, P., et al. 2023, *MNRAS*, 524, 6124
 Jakobsen, P., Ferruit, P., Alves de Oliveira, C., et al. 2022, *A&A*, 661, A80
 Jones, G. C., Bunker, A. J., Saxena, A., et al. 2024, *A&A*, 683, A238
 Jung, I., Finkelstein, S. L., Dickinson, M., et al. 2020, *ApJ*, 904, 144
 Jung, I., Finkelstein, S. L., Larson, R. L., et al. 2022, arXiv e-prints, arXiv:2212.09850
 Keating, L. C., Puchwein, E., Bolton, J. S., Haehnelt, M. G., & Kulkarni, G. 2024, *MNRAS*, 531, L34
 Kragh Jespersen, C., Steinhart, C. L., Somerville, R. S., & Lovell, C. C. 2024, arXiv e-prints, arXiv:2403.00050
 Larson, R. L., Finkelstein, S. L., Hutchison, T. A., et al. 2022, *ApJ*, 930, 104
 Laursen, P., Sommer-Larsen, J., & Razoumov, A. O. 2011, *ApJ*, 728, 52
 Lemos, P., Parker, L. H., Hahn, C., et al. 2023, in *Machine Learning for Astrophysics*, 18
 Leonova, E., Oesch, P. A., Qin, Y., et al. 2022, *MNRAS*, 515, 5790
 Lin, X., Cai, Z., Wu, Y., et al. 2024, *ApJS*, 272, 33
 Lin, Y., Oh, S. P., Furlanetto, S. R., & Sutter, P. M. 2016, *MNRAS*, 461, 3361
 Lu, T.-Y., Mason, C. A., Hutter, A., et al. 2024a, *MNRAS*, 528, 4872
 Lu, T.-Y., Mason, C. A., Mesinger, A., et al. 2024b, arXiv e-prints, arXiv:2411.04176
 Mason, C. A., Treu, T., Dijkstra, M., et al. 2018, *ApJ*, 856, 2
 McQuinn, M., Lidz, A., Zahn, O., et al. 2007, *MNRAS*, 377, 1043
 Mesinger, A., Aykutaalp, A., Vanzella, E., et al. 2015, *MNRAS*, 446, 566
 Mesinger, A. & Furlanetto, S. 2007, *ApJ*, 669, 663
 Mesinger, A., Furlanetto, S., & Cen, R. 2011, *MNRAS*, 411, 955
 Mesinger, A. & Furlanetto, S. R. 2008a, *MNRAS*, 385, 1348
 Mesinger, A. & Furlanetto, S. R. 2008b, *MNRAS*, 386, 1990
 Mesinger, A., Greig, B., & Sobacchi, E. 2016, *MNRAS*, 459, 2342
 Meyer, R., Oesch, P., Giovinazzo, E., et al. 2024, arXiv preprint arXiv:2405.05111
 Meyer, R. A., Laporte, N., Ellis, R. S., Verhamme, A., & Garel, T. 2021, *MNRAS*, 500, 558
 Miralda-Escudé, J. 1998, *ApJ*, 501, 15
 Morishita, T., Mason, C. A., Kreilgaard, K. C., et al. 2024, arXiv e-prints, arXiv:2412.04211
 Murray, S., Greig, B., Mesinger, A., et al. 2020, *The Journal of Open Source Software*, 5, 2582
 Nakane, M., Ouchi, M., Nakajima, K., et al. 2024, *ApJ*, 967, 28
 Napolitano, L., Pentericci, L., Santini, P., et al. 2024, *A&A*, 688, A106
 Neufeld, D. A. 1990, *ApJ*, 350, 216
 Neymer, M., Smith, A., Kannan, R., et al. 2024, *MNRAS*, 531, 2943
 Oesch, P. A., Brammer, G., van Dokkum, P. G., et al. 2016, *ApJ*, 819, 129
 Oesch, P. A., van Dokkum, P. G., Illingworth, G. D., et al. 2015, *ApJ*, 804, L30
 Orlitová, I., Verhamme, A., Henry, A., et al. 2018, *A&A*, 616, A60
 Park, J., Mesinger, A., Greig, B., & Gillet, N. 2019, *MNRAS*, 484, 933
 Planck Collaboration, Aghanim, N., Akrami, Y., et al. 2020, *A&A*, 641, A6
 Qin, Y., Mesinger, A., Bosman, S. E. I., & Viel, M. 2021, *MNRAS*, 506, 2390
 Qin, Y., Mesinger, A., Prelogović, D., et al. 2024, arXiv e-prints, arXiv:2412.00799
 Roberts-Borsani, G. W., Bouwens, R. J., Oesch, P. A., et al. 2016, *ApJ*, 823, 143
 Saxena, A., Robertson, B. E., Bunker, A. J., et al. 2023, *A&A*, 678, A68
 Sobacchi, E. & Mesinger, A. 2014, *MNRAS*, 440, 1662
 Stark, D. P., Ellis, R. S., Charlot, S., et al. 2017, *MNRAS*, 464, 469
 Stark, D. P., Ellis, R. S., Chiu, K., Ouchi, M., & Bunker, A. 2010, *MNRAS*, 408, 1628
 Stark, D. P., Ellis, R. S., & Ouchi, M. 2011, *ApJ*, 728, L2
 Steidel, C. C., Rudie, G. C., Strom, A. L., et al. 2014, *ApJ*, 795, 165
 Tacchella, S., Eisenstein, D. J., Hainline, K., et al. 2023, *ApJ*, 952, 74
 Tang, M., Stark, D. P., Chen, Z., et al. 2023, *MNRAS*, 526, 1657
 Tang, M., Stark, D. P., Ellis, R. S., et al. 2024a, *MNRAS*, 531, 2701
 Tang, M., Stark, D. P., Topping, M. W., Mason, C., & Ellis, R. S. 2024b, arXiv e-prints, arXiv:2408.01507
 Tilvi, V., Malhotra, S., Rhoads, J. E., et al. 2020, *ApJ*, 891, L10
 Treu, T., Trenti, M., Stiavelli, M., Auger, M. W., & Bradley, L. D. 2012, *ApJ*, 747, 27
 Umeda, H., Ouchi, M., Nakajima, K., et al. 2024, *ApJ*, 971, 124
 Verhamme, A., Garel, T., Ventou, E., et al. 2018, *MNRAS*, 478, L60
 Witsstok, J., Maiolino, R., Smit, R., et al. 2024a, arXiv e-prints, arXiv:2404.05724
 Witsstok, J., Smit, R., Saxena, A., et al. 2024b, *A&A*, 682, A40
 Witten, C., Laporte, N., Martin-Alvarez, S., et al. 2024, *Nature Astronomy*, 8, 384
 Yamada, T., Matsuda, Y., Kousai, K., et al. 2012, *ApJ*, 751, 29
 Zahn, O., Mesinger, A., McQuinn, M., et al. 2011, *MNRAS*, 414, 727
 Zitrin, A., Labbé, I., Belli, S., et al. 2015, *ApJ*, 810, L12

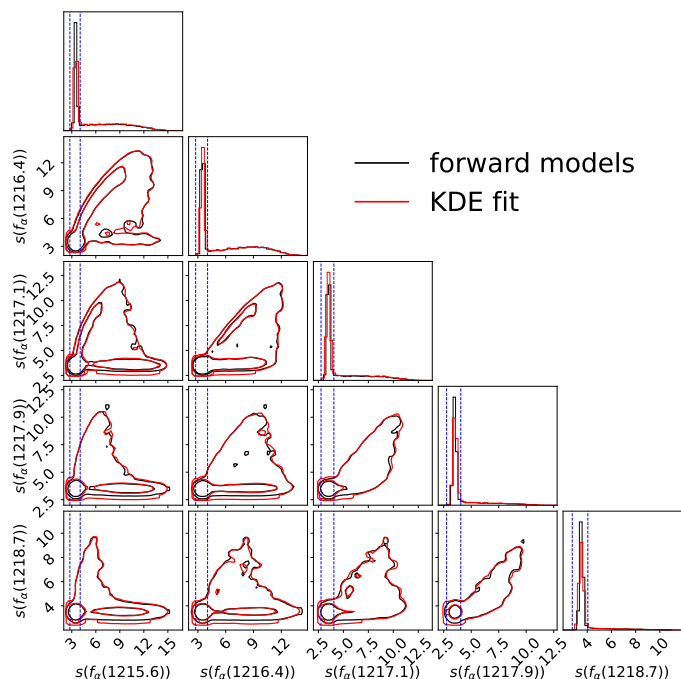


Fig. A.1. Corner plot of scaled flux spectra and the KDE fit to the forward models. Black contours represent 68% and 95% C.L. of the distribution of forward models for a galaxy located in the center of a $R_b = 10\text{cMpc}$ ionized bubble. Red contours represent same distributions for the KDE fit to the forward models. Blue dashed lines mark regions with $\pm 2\sigma$ of the noise of the spectrum. Contours outside of these dashed lines represent Lyman- α emission, with non-negligible correlation between bins.

Appendix A: Mapping the joint distribution over all flux bins with kernel density estimation

In Section 3 we showed how we generate forward models of JWST observations. Here we detail how we compute flux PDFs, i.e. likelihoods, in the space of local HII region parameters. In Fig. A.1 in black we show a corner plot of forward models of a galaxy located in the center of its local HII region with size $R_b = 10\text{cMpc}$. Black contours display 68% and 95% C.L. of the distribution respectively. We only show bins in our fiducial resolution ($R = 1000$) where the Lyman- α emission is located. In order to fit a density estimator to obtain a smooth PDF, we scale fluxes by a common function:

$$s(f_\alpha(\lambda)) = 93.5 + 5 \log(10^{-18} + 2f_\alpha(\lambda)). \quad (\text{A.1})$$

Each column and row represents one wavelength bin of the flux scaled by the function in Eq. A.1. We fit a Kernel Density Estimator to the forward models displayed in the corner plot with an exponential kernel of bandwidth $h = 0.12$. The scaling function and bandwidth were selected by optimizing the results of Section 4 (i.e., kernel density bandwidth and normalizing function that allows the inference of bubble properties for the least number of galaxies). We show contours of the fitted KDE in red in Fig. A.1.

Several features can be noted in Fig. A.1. Firstly, there is a strong peak for lower values of $s(f_\alpha(\lambda))$. This peak corresponds to the noise which is Gaussian by construction. This is further demonstrated with the blue dashed lines that show 5σ noise levels from Section 2.4. On the other hand, there are additional features for larger values of $s(f_\alpha(\lambda))$. These features represent

the Lyman- α signal that is higher than the noise. It is important to note that there is non-negligible correlation between different bins and the distribution is highly non-trivial. This shows that a simple likelihood that uses independent Gaussians for each bin would potentially bias the inference and an approach that fits the whole distribution is necessary.

KDE fits the data for all of the bins, in the noise and signal regimes. There is a small overestimation of the width of the distribution for bins that are noise-dominated. Since these bins do not give a lot of information for Lyman- α inference, our KDE is not biasing results.